

Image currents in azimuthally inhomogeneous metallic beam pipes

A. Mostacci*

Università degli studi di Roma "La Sapienza," Rome, Italy

(Received 9 June 2005; published 15 August 2005)

We consider an ultrarelativistic particle traveling on axis in an infinitely long cylindrical metallic beam pipe with azimuthally varying conductivity. For a circular geometry, a semi-analytical solution is obtained using the Green functions and applying approximate boundary conditions for conductors. The theory predicts an image current distribution on the pipe walls practically independent of the azimuth, at least in the frequency range relevant for future machines such as the LHC. Numerical electromagnetic simulations and bench measurements confirm the theoretical predictions. Implications for the beam-induced heating in the copper-coated, welded LHC beam screen are also addressed.

DOI: [10.1103/PhysRevSTAB.8.084402](https://doi.org/10.1103/PhysRevSTAB.8.084402)

PACS numbers: 41.75.-i, 41.20.-q

I. MOTIVATION AND GOALS

The Large Hadron Collider (LHC) beam screen [1] is copper coated to reduce resistive wall effects and the copper layer is $75 \mu\text{m}$ thick. The LHC beam pipe will reach cryogenic temperature (between 4 and 20 K) in the arcs. All along its length, the beam screen has a longitudinal welding strip which is about 1/60th of the entire pipe circumference. This strip is made of a conductor whose conductivity can be well approximated by the stainless steel one. Therefore the beam will "see" an azimuthally inhomogeneous pipe made for the greatest part by copper but with an azimuthally small piece of stainless steel (whose conductivity is much smaller than the copper one, especially at cryogenic temperature).

The distribution of the image currents is important to estimate the beam-wall interaction and heating power loss. In the LHC case, in fact, if the currents would avoid the badly conducting region and would flow mainly in the copper, the beam would practically not see any difference between a copper beam pipe and the welded one, at least concerning the heating power losses. The transverse beam dynamics, on the contrary, may be affected from the asymmetry of the image currents. For resistors in parallel this is the case: the currents somehow choose the less "dissipative" path and the resistors with lower resistivity carry the highest current (according to Ohm's law). On the contrary, if the image currents are constant over the azimuth, i.e., if the same amount of current flows in the copper and in the stainless steel, then the beam would dissipate a considerable power due to the weldings.

Beam pipes with azimuthally inhomogeneous resistivity are present also in other accelerators devices (e.g., some kicker magnets) and in this paper we propose a general method to address their effect on the beam. We consider a single relativistic particle traveling on axis in an infinitely long cylindrical metallic beam pipe, whose conductivity is varying with the azimuth. To achieve a (semi)analytical solution for the field inside the pipe (and the boundary current distribution), we consider boundary surface admittance varying sinusoidally with the azimuth. The parameter range considered in our examples concerns the LHC case, but the method is general and applicability limits of the approximations involved are discussed.

The fields inside the pipe can be derived from magnetic and electric Hertzian potentials (Sec. II), whose amplitudes depend on the driving term (the charge field) and on the boundary conditions. For metallic beam pipes, some simplified boundary conditions can be assumed. Such approximate conditions drastically simplify the problem which is reduced to the solution of a linear system of equations for the coefficients of a multipole expansion of the Hertzian

*Also at INFN, Laboratori Nazionali di Frascati, C.P. 13 00044 Frascati, Italy.
Electronic address: Andrea.Mostacci@uniroma1.it

potentials (Sec. III). The system is truncated to a given order and recurrence relations are found for the quantities needed to express the fields everywhere inside the beam pipe. The longitudinal and azimuthal currents are proportional, respectively, to the azimuthal and longitudinal magnetic field on the boundary and their behavior is discussed in Sec. IV and compared to more simplified approaches. Bench measurement and numerical simulation confirming the conclusions of the above theory were already discussed in Ref. [2]. In Sec. V, we review the bench measurement results giving a more detailed insight on the measurement technique adopted. Section VI briefly discuss how to apply the theoretical results to estimate the power loss in the actual LHC beam screen geometry.

II. A GREEN'S FUNCTION APPROACH

The Green's function method has been successfully applied to study the coupling impedance of discontinuities in perfectly conducting cylindrical beam pipes, either for a charge traveling on axis [3] or traveling off axis [4,5].

In this paper we are concerned with a single relativistic particle traveling in an infinitely long cylindrical (metallic) beam pipe whose conductivity is varying with the azimuth. The pipe has a radius $r = b$ and its thickness is assumed to be much greater of the skin depth at any relevant frequency.

The fields inside the beam pipe can be expressed as a function of the currents on the boundary through the Hertzian potentials (Sec. II A), i.e., the same used in a perfectly conducting beam pipe. To get the actual field solution, we need proper boundary conditions (metallic pipe with conductivity σ) which are discussed in Sec. II B. For reader convenience, in Appendix A we apply our formalism to few simpler cases, getting results well established in literature.

A. Hertzian potentials in a perfectly conducting circular waveguide

We consider only time harmonic electromagnetic fields with a time dependence specified by the complex factor $\exp(-j\omega t)$, which is omitted. In a stationary, linear, isotropic, homogeneous medium which is free of sources, Maxwell's equations read

$$\nabla \times \mathbf{E} = jkZ\mathbf{H} \quad \text{and} \quad \nabla \times \mathbf{H} = -jkY\mathbf{E}, \quad (1)$$

where \mathbf{E} , \mathbf{H} are the complex numbers representing the electric and magnetic fields, respectively, $Z = 1/Y = \sqrt{\mu/\varepsilon}$ is the intrinsic impedance of the medium, and $k = \omega\sqrt{\mu\varepsilon}$ is the propagation constant or wave number. The permittivity and permeability of the medium ε and μ may be complex, incorporating the effect of losses. In the particular case of a vacuum, $Z = Z_0 = 120\pi \Omega$, and we distinguish the corresponding parameters by the suffix "0". SI units are used throughout.

The field can be expressed through the magnetic and electric Hertzian potentials $\mathbf{\Pi}$ and $\tilde{\mathbf{\Pi}}$ as follows:

$$\mathbf{E} = (k^2 + \nabla\nabla\cdot)\mathbf{\Pi} - jkZ_0\nabla \times \tilde{\mathbf{\Pi}}, \quad (2a)$$

$$\mathbf{H} = -j\frac{k}{Z_0}\nabla \times \mathbf{\Pi} - (k^2 + \nabla\nabla\cdot)\tilde{\mathbf{\Pi}}. \quad (2b)$$

The Hertzian potentials must be solutions of the wave equation; having applied the separation of variables

$$\frac{1}{r} \frac{\partial}{\partial r} \left(r \frac{\partial \mathbf{\Pi}}{\partial r} \right) + \frac{\partial^2 \mathbf{\Pi}}{\partial z^2} + \left(k^2 - \frac{m^2}{r^2} \right) \mathbf{\Pi} = 0; \quad (3)$$

furthermore $\mathbf{\Pi}$ and $\partial\tilde{\mathbf{\Pi}}/\partial r$ must be continuous at the beam pipe radius $r = b$, as follows from

the relation of these functions to the electromagnetic field. We therefore seek these functions in the form [4,6]:

$$\Pi_z = \frac{Z_0}{4\pi k} \sum_{m=0}^{\infty} \cos(m\phi) \int_{-\infty}^{+\infty} F_m(\alpha) \begin{cases} J_m(\Omega r)H_m(\Omega b) \\ J_m(\Omega b)H_m(\Omega r) \end{cases} e^{j\alpha z} d\alpha \quad \begin{matrix} r < b, \\ r > b, \end{matrix} \quad (4a)$$

$$\tilde{\Pi}_z = \frac{1}{4\pi k} \sum_{m=1}^{\infty} \sin(m\phi) \int_{-\infty}^{+\infty} \frac{\tilde{F}_m(\alpha)}{\Omega} \begin{cases} J_m(\Omega r)H'_m(\Omega b) \\ J'_m(\Omega b)H_m(\Omega r) \end{cases} e^{j\alpha z} d\alpha \quad \begin{matrix} r < b, \\ r > b, \end{matrix} \quad (4b)$$

where J_m and $H_m = H_m^{(1)}$ are the Bessel and Hankel (first kind) functions of order m , $\Omega^2 = k^2 - \alpha^2$ and $F_m(\alpha)$, $\tilde{F}_m(\alpha)$ are the unknown coefficients. To build the field only the z components of the potentials are needed. A more general expression for the Hertzian potentials, would be with $\exp(jm\phi)$ instead of sine and cosine. Let us define the function $G_m(\alpha; r, b)$ such that

$$G_m(\alpha; r, b) = \begin{cases} J_m(\Omega r)H_m(\Omega b) & r < b, \\ J_m(\Omega b)H_m(\Omega r) & r > b, \end{cases} \quad (5)$$

which is continuous at $r = b$.

Such Hertzian potentials can be physically justified considering that a perfectly conducting boundary can be replaced by a sheet of currents radiating in the free space (equivalence principle); the field can then be described as the sum of terms weighted by F_m and \tilde{F}_m (strictly related to the currents) which depend on the boundary conditions.

When the potentials (and the derived fields) are used in a perfectly conducting waveguide, they give the usual modes: the TE modes are derived from Π_z while the TM modes from $\tilde{\Pi}_z$ [7]. In all the other boundary conditions, e.g., discontinuous perfectly conducting wall or continuous wall but with finite conductivity, the two potentials must be considered jointly.

The currents that can be excited by a single particle traveling with a phase velocity βc in an infinitely long structure are synchronous with the source and thus proportional to $\delta(\alpha - \omega/\beta c)$:

$$\left. \begin{aligned} F_m(\alpha) &= F_m \delta(\alpha - \omega/\beta c) \\ \tilde{F}_m(\alpha) &= \tilde{F}_m \delta(\alpha - \omega/\beta c) \end{aligned} \right\} \rightarrow \Omega = j \frac{k}{\beta \gamma}.$$

Eventually, the potentials become

$$\Pi_z = -\frac{j}{2\pi^2} \frac{Z_0}{k} \sum_{m=0}^{\infty} F_m \begin{cases} I_m(kr/\beta\gamma)K_m(kb/\beta\gamma) \\ I_m(kb/\beta\gamma)K_m(kr/\beta\gamma) \end{cases} \cos(m\phi) e^{jzk/\beta} \quad \begin{matrix} r < b, \\ r > b, \end{matrix} \quad (6a)$$

$$\tilde{\Pi}_z = \frac{j}{2\pi^2} \frac{\beta\gamma}{k} \sum_{m=1}^{\infty} \tilde{F}_m \begin{cases} I_m(kr/\beta\gamma)K'_m(kb/\beta\gamma) \\ I'_m(kb/\beta\gamma)K_m(kr/\beta\gamma) \end{cases} \sin(m\phi) e^{jzk/\beta} \quad \begin{matrix} r < b, \\ r > b. \end{matrix} \quad (6b)$$

To obtain the fields, one simply needs to use Eqs. (2) [1].

In the case of perfectly conducting walls, the surface (electric) current density J_S is equal to the discontinuity of the magnetic field at the boundary, i.e.,

$$J_{S_z} = H_\phi(b^+) - H_\phi(b^-) = -\frac{1}{2\pi^2} \sum_{m=0}^{\infty} \left[\frac{F_m}{b} + \frac{m}{\beta} \left(\frac{\beta\gamma}{kb} \right)^2 \tilde{F}_m \right] \cos(m\phi) e^{jzk/\beta}, \quad (7a)$$

$$J_{S_\phi} = H_z(b^-) - H_z(b^+) = \frac{1}{2\pi^2} \sum_{m=1}^{\infty} j \frac{\tilde{F}_m}{kb} \sin(m\phi) e^{jzk/\beta}, \quad (7b)$$

showing the strict relationship between F_m , \tilde{F}_m and the currents; $H_\phi(b^+)$ means $H_\phi(r \rightarrow b^+)$ and so on. In a nonperfect conductor, there are no surface currents, since the field is continuous

over the boundary. Nevertheless, when using some approximate boundary condition (see Sec. II B), surface currents may “appear,” but with an expression different from Eq. (7).

B. Approximate boundary conditions

Approximate boundary conditions provide a relationship between the electric and magnetic field on a chosen surface. A comprehensive treatment of those conditions is reported in Ref. [8] where applications and validity limits are also discussed.

We will limit ourselves to first order boundary conditions which are sometimes referred to as SIBC (standard impedance boundary condition). A more detailed discussion focused on the application of SIBC to our problem can be found in Ref. [1]. For a homogeneous body whose boundary is a coordinate surface in a (generic) system of orthogonal curvilinear coordinates, it can be shown that (on the boundary)

$$\mathbf{n} \times \mathbf{E} = Z \mathbf{n} \times (\mathbf{n} \times \mathbf{H}) \quad \text{with} \quad Z = \sqrt{\frac{\mu}{\varepsilon}} \quad (8)$$

at the first order in the penetration depth δ ; \mathbf{n} is the outward unit vector normal to the surface. These relations (and their equivalent forms) are usually quoted as “Leontovitch boundary conditions.” Equation (8) can model progressive changes in the material properties if the local value of Z is given at each point of the surface [8].

A surface subjected to an impedance boundary condition supports electric and magnetic currents (being \mathbf{n} the outward unit normal)

$$\mathbf{J}_{\text{Se}} = -\mathbf{n} \times \mathbf{H} \quad \text{and} \quad \mathbf{J}_{\text{Sm}} = \mathbf{n} \times \mathbf{E}, \quad (9)$$

respectively. These currents are strictly related because of Eq. (8):

$$\mathbf{J}_{\text{Se}} = \frac{1}{\eta} \mathbf{n} \times \mathbf{J}_{\text{Sm}} \quad \text{or} \quad \mathbf{J}_{\text{Sm}} = -\eta \mathbf{n} \times \mathbf{J}_{\text{Se}}, \quad (10)$$

so that in the solution of a boundary value problem it is sufficient to determine just one current.

On the surface of a lossy medium the conditions, under which Eq. (8) can be justified, have been discussed in Ref. [8]. Being $\lambda_0 = 2\pi/k_0$ the wavelength of the electromagnetic field and $N = \sqrt{\varepsilon_r \mu_r}$ the diffraction index (in the boundary material), the summary of the requirements is

- (i) On the surface the external field is slowly varying on a scale of λ_0 (e.g., no sharp edges).
- (ii) Any variation of the material properties is slow on a scale of the local wavelength in the material, i.e.,

$$|k_0^{-1} N^{-1} \nabla(\ln Z)| \ll 1. \quad (11)$$

- (iii) At each point of the material

$$|N| \gg 1. \quad (12)$$

- (iv) At each point of the material

$$|\text{Im}(N)| k_0 \rho \gg 1, \quad (13)$$

where ρ is the smallest radius of curvature or dimension of the body. Based on detailed examinations of computed data and comparisons with situations where exact results are known, the last two conditions are rewritten in [9] as

$$|N| \geq 10 \quad \text{and} \quad |\text{Im}(N)| k_0 \rho \geq 2.3. \quad (14)$$

In the following we will use the SIBC, i.e., Eq. (8), and the above equations fix the validity limit of our approximated boundary conditions. Dealing with good conductors the displacement current can be neglected compared to the conduction current (in our frequency range), that is

$$\varepsilon = \varepsilon_0 - \frac{\sigma}{j\omega} \approx \frac{j\sigma}{\omega}, \quad Y(\omega) = \frac{1}{Z} = \sqrt{\frac{\varepsilon}{\mu}} \approx j\sqrt{\frac{\sigma}{j\omega\mu}}; \quad (15)$$

this last assumption imposes an upper frequency limit weaker than the constraint imposed by Eqs. (12)–(14). The expression of the complex electrical permittivity ε depends on the time dependence of the field; for a time dependence of $\exp(j\omega t)$, ε is the complex conjugate of Eq. (15). The length of penetration of the field in a conductor is referred to as “skin depth” and is given by

$$\delta = \sqrt{\frac{2}{\omega\mu_0\sigma}} = \sqrt{2}|N^{-1}k_0^{-1}| \quad \text{since} \quad N = \sqrt{\frac{j\sigma}{\omega\varepsilon_0}} \quad (16)$$

for nonmagnetic conductors ($\mu_r = 1$). Therefore Eq. (11) states that the variation of material properties is slow on the scale of a skin depth, while Eq. (13) imposes that the minimum radius of curvature of the surface has to be much larger than the skin depth (at any relevant frequency).

C. Modeling the surface admittance

We deal with a conducting beam pipe whose conductivity σ is a function of the azimuth ϕ , but is constant in the radial and longitudinal direction. For the sake of simplicity, assuming for $\sigma = \sigma(\phi)$ a sinusoidal behavior, such as

$$\sigma(\phi) = \left[\frac{\sqrt{\sigma_{\max}} + \sqrt{\sigma_{\min}}}{2} + \frac{\sqrt{\sigma_{\max}} - \sqrt{\sigma_{\min}}}{2} \cos(n\phi) \right]^2, \quad (17)$$

the surface admittance is as well a function of ω and ϕ , that is

$$Y(\omega, \phi) = Y_0(\omega) + Y_n(\omega) \cos(n\phi) \quad (\Omega^{-1}); \quad (18)$$

n is the number of oscillations of the conductivity between σ_{\max} and σ_{\min} along the pipe circumference. Y_0 depends on the square root of the frequency, while Y_n/Y_0 is a purely geometrical factor:

$$Y_0(\omega) = \sqrt{\frac{j}{\omega\mu_0}} \frac{\sqrt{\sigma_{\max}} + \sqrt{\sigma_{\min}}}{2}, \quad (19a)$$

$$\frac{Y_n}{Y_0} = \frac{\sqrt{\sigma_{\max}} - \sqrt{\sigma_{\min}}}{\sqrt{\sigma_{\max}} + \sqrt{\sigma_{\min}}} \quad (19b)$$

from Eq. (15) and considering nonmagnetic conductors. Big changes in the conductivity imply values of Y_n/Y_0 near unity. For example if the conductivity varies from the one of copper (at room temperature) $\sigma_{\text{Cu}} = 6 \times 10^7$ S/m to the conductivity of the stainless steel $\sigma_{\text{Ss}} = 10^6$ S/m, then Y_n/Y_0 is ≈ 0.76 ; such a behavior of the conductivity σ is shown in Fig. 1.

Y_n/Y_0 “measures” the variation of conductivity along the azimuth ($Y_n/Y_0 = 0$ is a homogeneous conductor); our final solution is derived as an expansion in this parameter; when it approaches to unity, more high order terms are needed [10]. The penetration in the metal follows the skin depth: at a given frequency it is bigger in the worst conductor, as shown in Fig. 1 (dash-dotted line). Typical values are of the order of microns for copper and ten microns for stainless steel at 1 GHz.

Eventually to assess the applicability limits of the SIBCs, we will use Eq. (14), that is that the skin depth has to be smaller than the wavelength and than the radius of the pipe. For example using the numerical values given in Fig. 1, the lower limit in frequency is ≈ 1 kHz while the upper one is ≈ 200 THz (at least concerning the use of Leontovich boundary conditions).

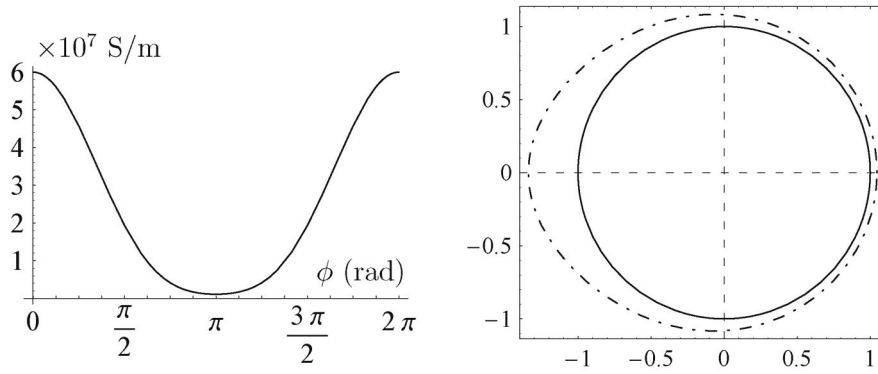


FIG. 1. Shape of the conductivity as a function of the azimuth ϕ (left plot) and corresponding behavior of the skin depth inside the conductor at 5 kHz (right plot). The conductivity varies from copper at room temperature ($\phi = 0$) to stainless steel ($\phi = \pi$). In the right plot, the black line represents the circular section of the pipe (in units of the radius) and the dash-dotted line is $\delta(\phi)/b$ away from it, where b is the pipe radius. ($b = 2$ cm, $\sigma_{\text{Cu}} = 6 \times 10^7$ S/m, $\sigma_{\text{ss}} = 10^6$ S/m).

III. FIELD SOLUTION FOR AZIMUTHALLY VARYING ADMITTANCE

A. System of equations

The fields E_ϕ, H_ϕ, E_z, H_z satisfy the boundary condition Eq. (8), that we may rewrite in our circular geometry (radius b) as

$$H_\phi|_{r=b} = Y(\omega, \phi)E_z|_{r=b}, H_z|_{r=b} = -Y(\omega, \phi)E_\phi|_{r=b}, \quad (20)$$

where the surface admittance $Y(\omega, \phi)$ is (co)sinusoidal in ϕ and given by Eq. (18). The fields involved in Eq. (20) are the total fields on the boundary, that is the sum of the scattered field and the field of the source. We will use the superscript “w” for the scattered field (e.g., H_ϕ^w) and the superscript “SC” (space charge) for the source field (e.g., H_ϕ^{SC}).

The scattered fields (on the boundary $r = b$) can be written [11] ($m = 1, 2, \dots$)

$$E_\phi^w|_{r=b} = -\frac{Z_0}{2\pi^2} E_\phi^m \sin(m\phi), \quad (21a)$$

$$E_z^w|_{r=b} = \frac{jZ_0}{2\pi^2} kb E_z^m \cos(m\phi) + \frac{jZ_0}{2\pi^2} jkb I_0 H_\phi^0, \quad (21b)$$

$$H_\phi^w|_{r=b} = \frac{H_\phi^m}{2\pi^2} \cos(m\phi) + \frac{(kb)^2}{2\pi^2} \left(\frac{\beta\gamma}{kb} I_0' \right) H_\phi^0, \quad (21c)$$

$$H_z^w|_{r=b} = -\frac{j}{2\pi^2} H_z^m \sin(m\phi), \quad (21d)$$

where the coefficients can be obtained by expressing the fields from Hertzian potentials:

$$H_\phi^0 = \frac{1}{b} \frac{F_0}{\beta^2 \gamma^2} K_0, \quad (22a)$$

$$E_\phi^m = \frac{m}{\beta} \frac{F_m}{b} I_m K_m - \tilde{F}_m I_m' K_m', \quad (22b)$$

$$H_\phi^m = \frac{kb}{\beta\gamma} \frac{F_m}{b} I_m' K_m - \frac{m}{\beta} \frac{\beta\gamma}{kb} \tilde{F}_m I_m K_m', \quad (22c)$$

$$E_z^m = \frac{1}{b} \frac{F_m}{\beta^2 \gamma^2} I_m K_m, \quad (22d)$$

$$H_z^m = \frac{\tilde{F}_m}{\beta\gamma} I_m K_m'. \quad (22e)$$

The arguments of the Bessel functions are always $kb/\beta\gamma$ and thus they have been omitted; the

exponential factor $\exp(jzk/\beta)$ is not included as well. The new variables $E_\phi^m, H_\phi^m, E_z^m, H_z^m$ have the dimension of a magnetic field in the Fourier space (that is C/m).

By substituting the last two equations (22d) and (22e) in Eqs. (22b) and (22c), we get

$$\frac{E_\phi^m - H_\phi^m}{(\beta\gamma)^2} = \left(\frac{m}{\beta} - \frac{kb}{\beta\gamma} \frac{I'_m}{I_m} \right) \left(E_z^m + \frac{H_z^m}{kb} \right), \quad (23a)$$

$$\frac{H_\phi^m}{(\beta\gamma)^2} = \frac{kb}{\beta\gamma} \frac{I'_m}{I_m} E_z^m - \frac{m}{\beta} \frac{H_z^m}{kb}, \quad (23b)$$

$$\frac{E_\phi^m}{(\beta\gamma)^2} = \frac{m}{\beta} E_z^m - \frac{I'_m}{I_m} \frac{H_z^m}{\beta\gamma}. \quad (23c)$$

The above quantities are limited and in general non-null, since they appear directly in the fields. The previous relations hold for any value of $kb/\beta\gamma$.

In the ultrarelativistic limit, the fields on the boundary are still given by Eqs. (21), with

$$I_0 \rightarrow 1 \quad \text{and} \quad \left(\frac{2\beta\gamma}{kb} I'_0 \right) \rightarrow 1. \quad (24)$$

Moreover, recalling that in this limit (for $m \geq 1$)

$$\frac{I'_m}{I_m} \left(\frac{kb}{\beta\gamma} \right) \approx m \frac{\beta\gamma}{kb} + \frac{1}{2(m+1)} \frac{kb}{\beta\gamma}, \quad (25)$$

we get, since $E_\phi^m/(\beta\gamma)^2 \rightarrow 0$,

$$H_\phi^m - E_\phi^m \approx -\frac{1}{2} \left[m + \frac{(kb)^2}{m+1} \right] \left(E_z^m + \frac{H_z^m}{kb} \right)$$

and

$$E_z^m \approx \frac{H_z^m}{kb},$$

which can be obtained also from $H_\phi^m/(\beta\gamma)^2 \rightarrow 0$. Eventually we can write

$$H_z^m = A_m (H_\phi^m - E_\phi^m) \quad \text{and} \quad E_z^m = \frac{A_m}{kb} (H_\phi^m - E_\phi^m), \quad (26)$$

where

$$A_m = \frac{(m+1)kb}{(kb)^2 + m(m+1)}; \quad (27)$$

thus all the coefficients of the field on the boundary [see Eq. (21)] are now expressed in terms of the new variables H_ϕ^m and E_ϕ^m ; we are actually changing variables from F_m, \tilde{F}_m to H_ϕ^m, E_ϕ^m . The proportionality between the E_z^m and H_z^m agrees with the multipole field obtained in [12] [Eq. (2.34), p. 52] by solving the Maxwell equations written for a particle traveling at the speed of light.

For an ultrarelativistic particle traveling on axis the longitudinal electric field vanishes, that is [Eqs. (A3)]

$$H_\phi^{\text{SC}} \approx \frac{Q}{2\pi b} \quad \text{and} \quad E_z^{\text{SC}} \approx 0, \quad (28)$$

Q being the charge of the particle(s) and having dropped the propagation (phase) factor.

Writing the fields in boundary condition of Eq. (20), considering n sinusoidal oscillation in the surface admittance [Eq. (19)] and equating the coefficients of sine (cosine) of the same order, a system of equations can eventually be written as follows:

$$\frac{(kb)^2}{2} H_\phi^0 = Z_0 Y_0 \left(jkb H_\phi^0 + \frac{2\pi^2}{Z_0} E_z^{\text{SC}} + \frac{Y_n}{2Y_0} jkb E_z^n \right) - 2\pi^2 H_\phi^{\text{SC}}, \quad (29a)$$

$$H_\phi^n = Z_0 Y_0 \left(jkb E_z^n + \frac{Y_n}{2Y_0} jkb E_z^{2n} + \frac{Y_n}{Y_0} \frac{2\pi^2}{Z_0} E_z^{\text{SC}} + \frac{Y_n}{Y_0} jkb H_\phi^0 \right), \quad (29b)$$

$$-jH_z^n = Z_0 Y_0 \left(E_\phi^n + \frac{Y_n}{2Y_0} E_\phi^{2n} \right), \quad (29c)$$

$$H_\phi^n = Z_0 Y_0 \left[jkb E_z^n + jkb \frac{Y_n}{2Y_0} E_z^{(t-1)n} + jkb \frac{Y_n}{2Y_0} E_z^{(t+1)n} \right] \quad t = 2, 3, \dots, \quad (29d)$$

$$-jH_z^n = Z_0 Y_0 \left[E_\phi^n + \frac{Y_n}{2Y_0} E_\phi^{(t-1)n} + \frac{Y_n}{2Y_0} E_\phi^{(t+1)n} \right] \quad t = 2, 3, \dots \quad (29e)$$

The forcing terms are the components of the charge field while the unknowns are only H_ϕ^0 , H_ϕ^{kn} and E_ϕ^{kn} ($k = 1, 2, \dots$). One can see [1] that orders different from kn give no contribution to the final solution. The system has a quite regular structure, except for the 0th and the 1st orders where the source terms appear and since there is no term in E_ϕ^m analogous to H_ϕ^0 (the azimuthal electric field has a null average along the azimuth). Each equation of the system relates the term of order tn to only terms of order $(t-1)n$ and $(t+1)n$; this symmetry will be exploited in the solution.

Inserting Eq. (26) into Eqs. (29), we can rewrite the system in the two variables that we will actually use to solve it, that is H_ϕ^n and E_ϕ^n .

(i) Zeroth order

$$\frac{(kb)^2}{2} H_\phi^0 + 2\pi^2 H_\phi^{\text{SC}} = Z_0 Y_0 \left[jkb H_\phi^0 + \frac{2\pi^2}{Z_0} E_z^{\text{SC}} + j \frac{Y_n}{2Y_0} A_n (H_\phi^n - E_\phi^n) \right]. \quad (30)$$

(ii) First Order

$$(1 - jZ_0 Y_0 A_n) H_\phi^n + jZ_0 Y_0 A_n E_\phi^n = Z_0 Y_0 \left(\frac{Y_n}{Y_0} \frac{2\pi^2}{Z_0} E_z^{\text{SC}} + \frac{Y_n}{Y_0} jkb H_\phi^0 \right) + jZ_0 Y_0 \frac{Y_n}{2Y_0} A_{2n} (H_\phi^{2n} - E_\phi^{2n}), \quad (31a)$$

$$A_n H_\phi^n - (A_n + jZ_0 Y_0) E_\phi^n = jZ_0 Y_0 \frac{Y_n}{2Y_0} E_\phi^{2n}. \quad (31b)$$

(iii) Order t ($t = 2, 3, \dots$)

$$(1 - jZ_0 Y_0 A_{tn}) H_\phi^n + jZ_0 Y_0 A_{tn} E_\phi^n = j \frac{Y_n}{2Y_0} Z_0 Y_0 A_{(t-1)n} [H_\phi^{(t-1)n} - E_\phi^{(t-1)n}] + j \frac{Y_n}{2Y_0} Z_0 Y_0 A_{(t+1)n} [H_\phi^{(t+1)n} - E_\phi^{(t+1)n}], \quad (32a)$$

$$A_{tn} H_\phi^n - (A_{tn} + jZ_0 Y_0 E_\phi^n) = j \frac{Y_n}{2Y_0} Z_0 Y_0 E_\phi^{(t-1)n} + j \frac{Y_n}{2Y_0} Z_0 Y_0 E_\phi^{(t+1)n}. \quad (32b)$$

B. Recursive solution of the system

The system of Eqs. (30)–(32) is, in general, of infinite dimension and it is not diagonal: an analytical solution is therefore impossible. We may truncate it at a given order L , that is $H_\phi^n = E_\phi^n = 0$ for any $t > L$. Then exploiting the symmetries of the system, we can build a recursive solution. Considering Eqs. (32), the variable at the order t depends on both the orders $(t-1)$

and $(t + 1)$. We can write for $t = 2, 3, \dots$

$$H_\phi^m = \frac{Y_n}{2Y_0} C_m H_\phi^{(t-1)n} + \frac{Y_n}{2Y_0} D_m E_\phi^{(t-1)n}, \quad (33a)$$

$$E_\phi^m = \frac{Y_n}{2Y_0} E_m H_\phi^{(t-1)n} + \frac{Y_n}{2Y_0} G_m E_\phi^{(t-1)n}, \quad (33b)$$

where the dependence on the $(t + 1)$ variable is hidden in the coefficients C, D, E, G , as it will become clearer later. The azimuthal change of the conductivity is directly related to $Y_n/2Y_0$. No assumption has been made in writing Eqs. (33) but neither any step towards the final solution. Using Eqs. (33) to write the $(t + 1)$ variables as functions of the t variables and substituting in Eqs. (32), we get

$$\begin{pmatrix} M_{11} & M_{12} \\ M_{21} & M_{22} \end{pmatrix} \begin{pmatrix} H_\phi^m \\ E_\phi^m \end{pmatrix} = j \frac{Y_n}{2Y_0} Z_0 Y_0 \begin{pmatrix} A_{(t-1)n} & -A_{(t-1)n} \\ 0 & 1 \end{pmatrix} \begin{pmatrix} H_\phi^{(t-1)n} \\ E_\phi^{(t-1)n} \end{pmatrix}. \quad (34)$$

The elements of the matrix \mathbf{M} are

$$M_{11} = 1 - jZ_0 Y_0 A_m - jZ_0 Y_0 \left(\frac{Y_n}{2Y_0} \right)^2 A_{(t+1)n} [C_{(t+1)n} - E_{(t+1)n}], \quad (35a)$$

$$M_{12} = jZ_0 Y_0 \left\{ A_m + \left(\frac{Y_n}{2Y_0} \right)^2 A_{(t+1)n} [D_{(t+1)n} - G_{(t+1)n}] \right\}, \quad (35b)$$

$$M_{21} = A_m - j \left(\frac{Y_n}{2Y_0} \right)^2 Z_0 Y_0 E_{(t+1)n}, \quad (35c)$$

$$M_{22} = -A_m - jZ_0 Y_0 \left[1 + \left(\frac{Y_n}{2Y_0} \right)^2 G_{(t+1)n} \right], \quad (35d)$$

where the coefficients of order $(t + 1)$ come from having written Eqs. (33) for $H_\phi^{(t+1)n}$ and $E_\phi^{(t+1)n}$. Therefore, Eq. (34) is simply a 2×2 system where the ‘‘unknowns’’ are H_ϕ^m, E_ϕ^m and the $H_\phi^{(t-1)n}, E_\phi^{(t-1)n}$ may be considered as driving terms. Inverting the matrix \mathbf{M} and after some algebra, we get the following recurrence relations:

$$C_m = -j \frac{Z_0 Y_0}{\Delta_t} A_{(t-1)n} \left\{ A_m + jZ_0 Y_0 \left[1 + \left(\frac{Y_n}{2Y_0} \right)^2 G_{(t+1)n} \right] \right\}, \quad (36a)$$

$$D_m = j \frac{Z_0 Y_0}{\Delta_t} \left\{ A_m A_{(t-1)n} + jZ_0 Y_0 [A_{(t-1)n} - A_m] + jZ_0 Y_0 \left(\frac{Y_n}{2Y_0} \right)^2 \{ A_{(t-1)n} G_{(t+1)n} - A_{(t+1)n} [D_{(t+1)n} - G_{(t+1)n}] \} \right\}, \quad (36b)$$

$$E_m = -j \frac{Z_0 Y_0}{\Delta_t} \left[A_{(t-1)n} A_m - jZ_0 Y_0 \left(\frac{Y_n}{2Y_0} \right)^2 A_{(t-1)n} E_{(t+1)n} \right], \quad (36c)$$

$$G_m = j \frac{Z_0 Y_0}{\Delta_t} \left\{ A_m A_{(t-1)n} + 1 - jZ_0 Y_0 A_m - jZ_0 Y_0 \left(\frac{Y_n}{2Y_0} \right)^2 \{ A_{(t-1)n} E_{(t+1)n} + A_{(t+1)n} [C_{(t+1)n} - E_{(t+1)n}] \} \right\}, \quad (36d)$$

where

$$\Delta_t = \det(\mathbf{M}) = M_{11} M_{22} - M_{12} M_{21}. \quad (37)$$

The initial condition of such a recurrence relation is simply given by the truncation of the system at a given order $t = L$, that is

$$C_{(L+1)n} = D_{(L+1)n} = E_{(L+1)n} = G_{(L+1)n} = 0. \quad (38)$$

To summarize, once fixed the order of truncation L the coefficients C_m, D_m, E_m , and G_m can be computed by using Eqs. (36) with the initial condition given by Eq. (38). Then, applying

Eqs. (33), H_ϕ^n and E_ϕ^n are known once determined $H_\phi^{(t-1)n}$ and $E_\phi^{(t-1)n}$, for $t \geq 2$. Therefore the next step is to find H_ϕ^0 , H_ϕ^n , and E_ϕ^n which are directly dependent on the source H_ϕ^{SC} , E_z^{SC} , as shown in Eqs. (30) and (31).

Writing H_ϕ^n and E_ϕ^n according to Eqs. (33), we can write Eqs. (31) as

$$\mathbf{M} \begin{pmatrix} H_\phi^n \\ E_\phi^n \end{pmatrix} = j \frac{Y_n}{Y_0} Z_0 Y_0 \begin{pmatrix} A_0 & 0 \\ 0 & 0 \end{pmatrix} \left\{ (kb)^2 H_\phi^0 - j \frac{2\pi^2}{Z_0} kb E_z^{\text{SC}} \right\}, \quad (39)$$

where the elements of the matrix \mathbf{M} are again given by Eqs. (35), but now considering $t = 1$ and $A_0 = 1/(kb)$, following Eq. (27). Eventually solving this 2×2 system, we get

$$H_\phi^n = \frac{Y_n}{Y_0} C_n (kb)^2 H_\phi^0 \quad \text{and} \quad E_\phi^n = \frac{Y_n}{Y_0} E_n (kb)^2 H_\phi^0, \quad (40)$$

neglecting E_z^{SC} in the ultrarelativistic limit of Eq. (28); the coefficients C_n and D_n are then given by Eqs. (36), assuming $t = 1$. Strictly speaking, Eqs. (36) hold only for $t \geq 2$; nevertheless for sake of simplicity and in view of a later computation we can redefine C_{tn} , D_{tn} , E_{tn} , and G_{tn} such as that they obey Eqs. (36) for $t \geq 1$ with the additional condition

$$D_n = G_n = 0. \quad (41)$$

This ‘‘asymmetry’’ between the coefficients takes into account that E_ϕ has zero average over the azimuth ($E_\phi^n = 0$). Eventually, Eq. (30) becomes

$$H_\phi^0 = -2\pi^2 H_\phi^{\text{SC}} \left[\frac{(kb)^2}{2} - jkbZ_0Y_0 - jZ_0Y_0 \left(\frac{Y_n}{2Y_0} \right)^2 2A_n(C_n - E_n)(kb)^2 \right]^{-1}, \quad (42)$$

where H_ϕ^{SC} is given by Eq. (28).

The solution is now complete. It is not known in a closed analytical formula, but nevertheless it can be computed. Once chosen the value of L , according to the desired degree of approximation, the solution can be obtained by going through the following steps:

- (1) Compute C_{tn} , D_{tn} , E_{tn} , and G_{tn} using Eqs. (36) for $t \geq 1$, with initial conditions given by Eqs. (38) and (41).
- (2) After having obtained H_ϕ^0 from Eqs. (42), compute H_ϕ^{tn} and E_ϕ^{tn} from Eqs. (33) and (40).
- (3) Compute the scattered field on the boundary with Eqs. (21) and (26), keeping in mind that $m = tn$ with $t = 1, 2, \dots$.

The accuracy of the solution obtained depends on the order L where the system of Eqs. (30)–(32) is truncated. In principle, if the system is truncated at order L , the boundary conditions are satisfied up to order $(L - 1)n$; this means that the quantity

$$\mathcal{E}_\phi = \left| \frac{H_\phi^L - Y(\omega)E_z^L}{H_\phi^{\text{SC}}} \right|_{r=b} \quad (43)$$

is proportional to $\cos(L\phi)$. The superscript L recalls that the solution is approximated to order L and thus that the fields are sinusoidal functions of $tn\phi$ with $t = 0, \dots, L$. The same conclusion applies to

$$\mathcal{E}_z = \left| \frac{H_z^L + Y(\omega)E_\phi^L}{H_z^n} \right|_{r=b} \quad (44)$$

which is proportional to $\sin(L\phi)$. Equations (43) and (44) are simply the ratio between the term not satisfying a boundary condition and the amplitude of the lower order term of the fields involved in that boundary condition. Equations (43) and (44) may be used to assess the validity of the solution (Appendix B).

Once the fields at the boundary are known, one can easily derive the fields in any point inside the circular beam pipe; interested reader can find the expression in [1]. In this paper we will limit our analysis at the image current distributions (i.e., fields on the boundary) which are interesting to estimate the heating and beam power losses.

IV. THEORETICAL RESULTS

Applying the results of the previous section, the field solution can be found analytically only for truncation indexes L of the order of few units and therefore it is accurate only for small changes in conductivity (i.e., $Y_n/Y_0 \ll 1$), which is not our practical case. In this section we will present numerical results taking, as an example, parameters relevant for the LHC beam screen, where the conductivity varies from the copper one ($\sigma_{\text{Cu}} = 6 \times 10^7$ S/m at room temperature) to the stainless steel one ($\sigma_{\text{ss}} = 10^6$ S/m), which correspond to $Y_n/Y_0 = 0.76$. Moreover the LHC will operate at cryogenic temperatures, where the conductivity σ of copper increases roughly by a factor 100, while electric properties of the stainless steel remain the same; this bigger variation in conductivity implies a Y_n/Y_0 much closer to unity, that is $Y_n/Y_0 = 0.97$. It is worth mentioning that in this case the lower frequency validity limit of SIBCs of Eq. (8) is now given by Eq. (11), that is a limitation on the spatial derivatives of $Y(\omega)$; the upper frequency limit is unchanged since it is related to the region with the worst conductivity. All the numerical examples will deal with both the above values of Y_n/Y_0 and $n = 1$ since only one welding is present in the LHC beam screen.

We will show the model predictions for the fields on the boundary and compare them to some approximated approaches. The system must be truncated in order to be solved, convergence and validity issues of such solution are addressed in Appendix B.

A. Fields on the boundary

The surface density of the currents supported by the conductor is proportional to the magnetic field on the boundary, as stated in Eq. (9). The behavior of H_ϕ (the longitudinal current) is presented in Fig. 2 for various frequencies and for two different $\sigma(\phi)$; it is practically constant up to very low frequencies where the field (and the current) decreases in the worst conductor. The variation of the field is increasing with Y_n/Y_0 , but the effect on H_ϕ is remarkable only at low frequencies. This is a first result important for practical cases (e.g., LHC): the current avoids the “bad” conductor only at very low frequencies and this may have consequences in the final design.

To check if there is any evidence of azimuthal currents, one should look to H_z , which is proportional to them. The longitudinal magnetic field is negligible with respect to H_ϕ (4 orders

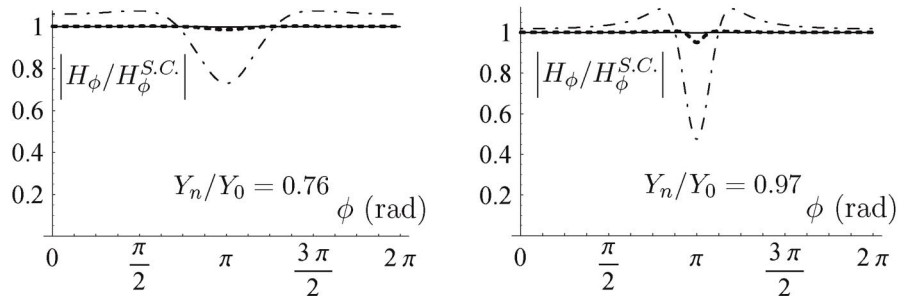


FIG. 2. Azimuthal magnetic field on the boundary ($r = b$). The field is plotted at different frequencies: 1 GHz (solid line), 1 MHz (thick dashed line), 1 kHz (dot-dashed line) for two different variations of the conductivity. At the higher frequency the field is more or less constant and the solid lines are hardly visible. Increasing the variation in the conductivity, H_ϕ at the center of the worst conductor decreases, but this is remarkable only at low frequencies. ($b = 2$ cm, $n = 1$).

of magnitude of difference) and it is strongly decreasing with frequency; moreover it does not seem to depend on the jump in the conductivity [1].

The longitudinal electric field is found to be maximum in the worst conductor ($\phi = \pi$ if $n = 1$), as shown in Fig. 3 for two different jumps in the conductivity: the peak of the field is narrower for bigger variations in the conductivity, while its maximum seems not to be very much affected (at least in the examples shown). As we may expect, the longitudinal field is decreasing at lower frequencies. In fact it is worth reminding that the average value (over ϕ) of E_z is constant with the radius [1] and thus it is equal to the longitudinal electric field on the z axis which is the longitudinal coupling impedance per unit length and unit charge [5]. The ϕ average of E_z is proportional to the area of the curve representing the longitudinal electric field: it is smaller for the “cold” copper (that is more conducting than at room temperatures) and this is physically sound.

The frequency range of interest for an LHC-like case is up to a few GHz and in this range the azimuthal magnetic field is constant, while the longitudinal electric field has its maximum in the “badly” conducting region. The quantities

$$\frac{|\Delta H_\phi|}{|H_\phi|_{\max}} = \frac{|H_{\phi \max} - H_{\phi \min}|}{|H_\phi|_{\max}}, \quad (45a)$$

$$\frac{|\Delta E_z|}{|E_z|_{\max}} = \frac{|E_{z \max} - E_{z \min}|}{|E_z|_{\max}}, \quad (45b)$$

will be small when the field is constant (over the azimuth), while they can (in principle) reach unity, when the field varies strongly with ϕ . The situation is sketched in Fig. 4 in a wide range of frequencies for $Y_n/Y_0 = 0.76$. The shaded regions highlight where the assumed SIBCs of Eq. (8) are not strictly valid.

The solid line is the normalized variation of E_z while the dashed line refers to H_ϕ . The curves cross each other at two frequencies; between them the azimuthal magnetic field remains approximately constant (see Figs. 2 and 3) while below the lower frequency and above the higher one, E_z is constant and H_ϕ varies with the azimuth. Such frequencies vary only a little with Y_n/Y_0 ; for example, keeping fixed the lower conductivity (stainless steel) and varying the maximum one from cold copper ($Y_n/Y_0 = 0.97$) to half of the copper conductivity at room temperature ($Y_n/Y_0 = 0.68$), the crossing frequencies remain around 100 Hz and 1 THz. The curves vary from a minimum value that is practically zero to a maximum (identical for both curves) that is 0.864 in the example of Fig. 4 ($Y_n/Y_0 = 0.76$). This maximum value is related to the variation in the conductivity, namely Y_n/Y_0 ; when the latter approaches unity, the maximum value grows (for instance it is 0.986 when $Y_n/Y_0 = 0.97$), but remains constant for both curves. Analogously when Y_n/Y_0 decreases, the plateau value decreases as well (e.g., for $Y_n/Y_0 = 0.68$

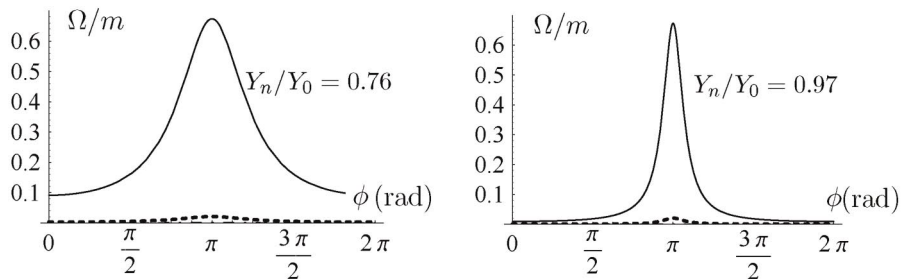


FIG. 3. Longitudinal electric field on the boundary ($r = b$) per unit charge. The absolute value of the field is plotted at different frequencies: 1 GHz (solid line), 1 MHz (thick dashed line), 1 kHz (dot-dashed line) for two different variations of the conductivity. The field at 1 kHz is 4 orders of magnitudes smaller than at 1 GHz and the dot-dashed lines lie on the horizontal ϕ axis (and they are not visible). The area of the curve is 2π the coupling impedance per unit length. ($b = 2$ cm, $n = 1$).

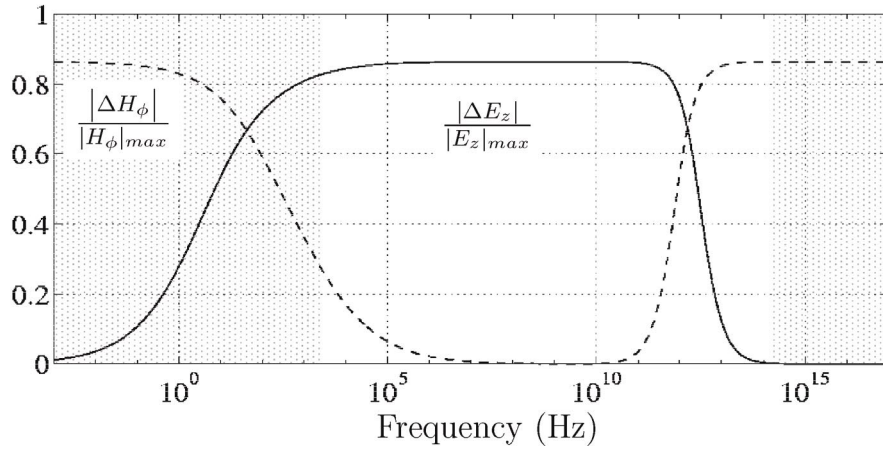


FIG. 4. Variation of the H_ϕ and E_z on the surface of the conductor, normalized to their maximum values (on the boundary). The frequency is in logarithmic scale. In the shaded regions, the approximate boundary conditions assumed are not strictly valid. ($b = 2$ cm, $n = 1$).

it is at 0.808). Plotting for those three cases the normalized variation of H_ϕ as a function of the normalized variation of E_z , we get Fig. 5.

By increasing Y_n/Y_0 , the curves tend to have a squared shape. The solid lines represent the path of a point going clockwise from low frequency (i.e., starting from $\Delta E = 0$ that is the y axis) to ≈ 10 GHz (where $\Delta H = 0$ on the x axis); then increasing the frequency from ≈ 10 GHz the points follow the dashed lines in the opposite direction ending again on the y axis where $\Delta E = 0$ (according to Fig. 4).

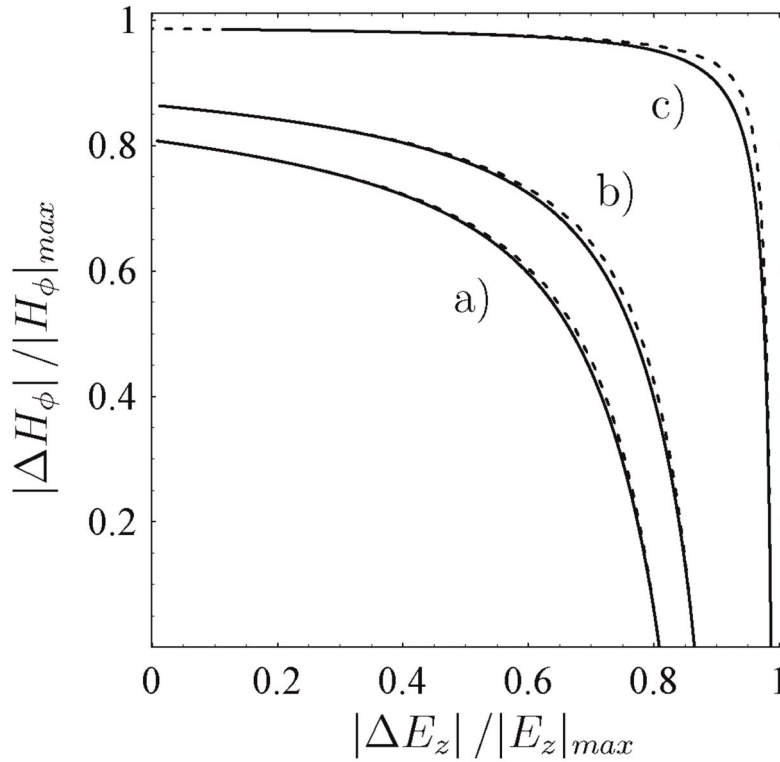


FIG. 5. Normalized variation of the azimuthal magnetic field versus the normalized variation of the longitudinal electric field. The three sets of curves refer to different conductivity jumps: for the curves (a) $Y_n/Y_0 = 0.68$, for (b) $Y_n/Y_0 = 0.76$ while for (c) $Y_n/Y_0 = 0.97$. ($b = 2$ cm, $n = 1$).

The solution for very low and very high frequency limit have been discussed as well in Ref. [1], keeping in mind that those regimes are at the edge (high frequencies) or outside (low frequencies) the validity limit of the SIBCs (shaded region in Fig. 4). For example, at high frequencies the electric field is proportional to $1/\omega$ and its value does not depend on the conductivity [12,13]; this behavior is met by our solution for frequencies above 10 THz in our geometry. Anyway, it should be reminded that at so high frequency, the skin depth becomes comparable with the mean free path length of the conduction electrons inside the metal and the anomalous skin effect (not included in the theory) should be considered [14]. In fact for metals at cryogenic temperature (much longer mean free paths) the anomalous skin effect starts in the GHz range. Instead, at low frequency, even if the SIBC are not anymore strictly valid, one can infer that the surface currents behave accordingly to Ohm's law, i.e., they flow mainly in the better conducting region, as shown in [1].

B. Other approximate solutions

In the following we compare the “complete” semianalytical solution of the previous section with other two approaches. The first one, called “analytical” solution, is obtained by assuming *a priori* the number of relevant ϕ -harmonics and then solving analytically the resulting system. On the contrary, the “perturbative” solution assumes that the magnetic field on the boundary is identical to the field of a beam in the free space.

The analytical solution for of order 3 (and $n = 1$) can be found with a reasonable effort the results are presented is plotted in Figs. 6 and 7 for $Y_n/Y_0 = 0.76$ and high β (red lines) to be compared with the previous complete solution (green lines). The electric field agrees quite well

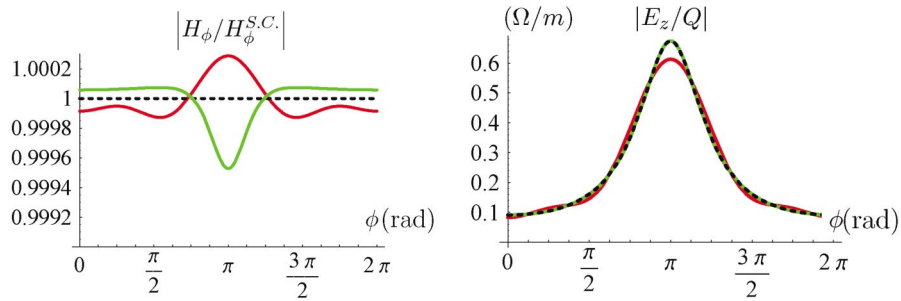


FIG. 6. (Color) Azimuthal magnetic field and longitudinal electric field on the boundary at 1 GHz. The dashed black line is the result of the perturbative approach. The red line is an analytical solution including only the first three ϕ harmonics for $\beta = 0.999\,999$ and the green one is the complete solution. ($b = 2$ cm, $n = 1$).

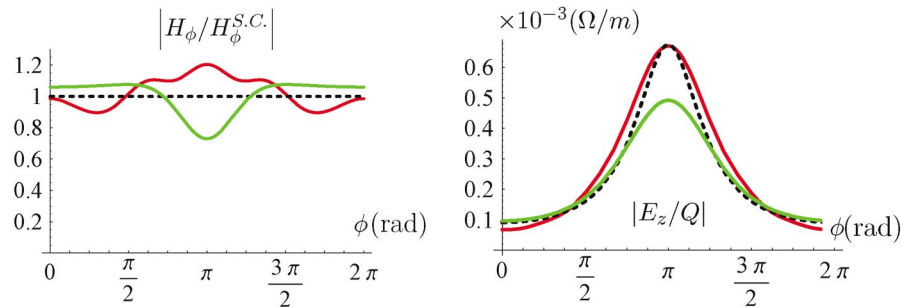


FIG. 7. (Color) Azimuthal magnetic field and longitudinal electric field on the boundary at 1 kHz. The dashed black line is the result of the perturbative approach. The red line is an analytical solution including only the first three ϕ -harmonics for $\beta = 0.999\,999$ and the green one is the complete solution. ($b = 2$ cm, $n = 1$)

at low and at high frequency, while the azimuthal magnetic field is quite different at low frequencies (note the different scales of the figures). Obviously these fields do not fulfill exactly the boundary conditions. A first order perturbative solution is plotted as well (black dashed lines): the azimuthal magnetic field on the boundary is assumed equal to the the field of the charge in the perfectly conducting pipe (H_ϕ^{SC}) and the longitudinal electric field is $E_z \approx ZH_\phi^{SC}$ from SIBC of Eq. (8). The agreement is good at high frequency, when the azimuthal magnetic field is actually constant. One can use the good previous statement as a first step of an iterative solution; anyway to get the complete value of the H_ϕ one has to make many iterations and the final solution has a complexity analogous to our solution. Decreasing the relativistic β the behavior does not change significantly, at least in the GHz range [1].

V. EXPERIMENTAL RESULTS

In the previous sections we have discussed a semianalytical field solution for a metallic, infinitely long beam pipe with an sinusoidal azimuthal variation of conductivity. In the part of the spectrum practically relevant (at least for the LHC), the magnetic field on the boundary (i.e., the image currents) is found to be independent of the azimuth. The solution tends to a DC-like behavior (image currents avoiding the bad conducting part) only for extremely low frequencies (see Fig. 4). This is consistent with a first order perturbative approach, i.e., assuming on the boundary the same magnetic field as for a charge in the free space, which is now fully justified (see Fig. 6). To assess these results, numerical simulations and bench measurements have been performed independently [1,2].

Numerical simulation used the High Frequency Structure Simulator (HFSS) [15], a general purpose electromagnetic fields simulator. A first simulation concerned a metallic beam pipe made of 16 slices of different conductivity approximating the $\sigma(\phi)$ of Fig. 1. To achieve more accurate results, a pipe done of four alternate slices of different metals (two slices of copper and two slices of stainless steel) has been simulated as well. The simulation technique and the results have been extensively discussed in Refs. [1,2]. In both cases the magnetic field has been found azimuthal ($H_\phi \gg H_z$) and constant along the azimuth as predicted from the theory.

A. Measurement setup

A cylindrical pipe made of 12 different bars which can be mounted and dismounted within a reasonable mechanical precision, has been designed and built (see Fig. 8). Each bar is “identical” to the others in shape, so that they can be interchanged; they are kept in place by external rings with screws. There are four of such rings, since the entire structure is 70 cm long (see Fig. 9); the distance between two opposite bars is fixed (to 5 cm) by using external metallic pieces as reference (not shown). The bars are available in two sets, one set of 12 steel bars (bad conductor) and one set of 12 brass bars (good conductor). The prototype can be mounted in all possible combinations, from all brass bars to all steel bars. For instance in Fig. 8, the pipe is mounted using six brass bars (yellow ones) and six steel bars (gray ones) alternatively, while in Fig. 9 all the 12 brass bars are placed.

To make precise, reliable, and meaningful bench measurements, the pipe has been transformed into a TEM resonator by inserting a cylindrical tube (silver-plated stainless steel) along the axis of the structure; the inner cylinder is kept in the right position by proper Teflon supports (see Fig. 9, lower right photo). The diameter of the silver-plated tube is 1 cm and its length is 50 cm; it is chosen of stainless steel to ensure mechanical stability and it is silver plated to reduce ohmic losses. The coupling circuit is shown in Fig. 9 (lower left); the little disk on the edge of the electrode increases the coupling capacity, giving stability to the resonance frequency with respect to the positioning of the coupling circuit.

If the azimuthal magnetic field along the pipe circumference is constant, the power loss inside our cavity will be simply the sum of the power dissipated in the inner conductor and the power dissipated in each of the 12 bars making up the pipe. Then exchanging a good conducting

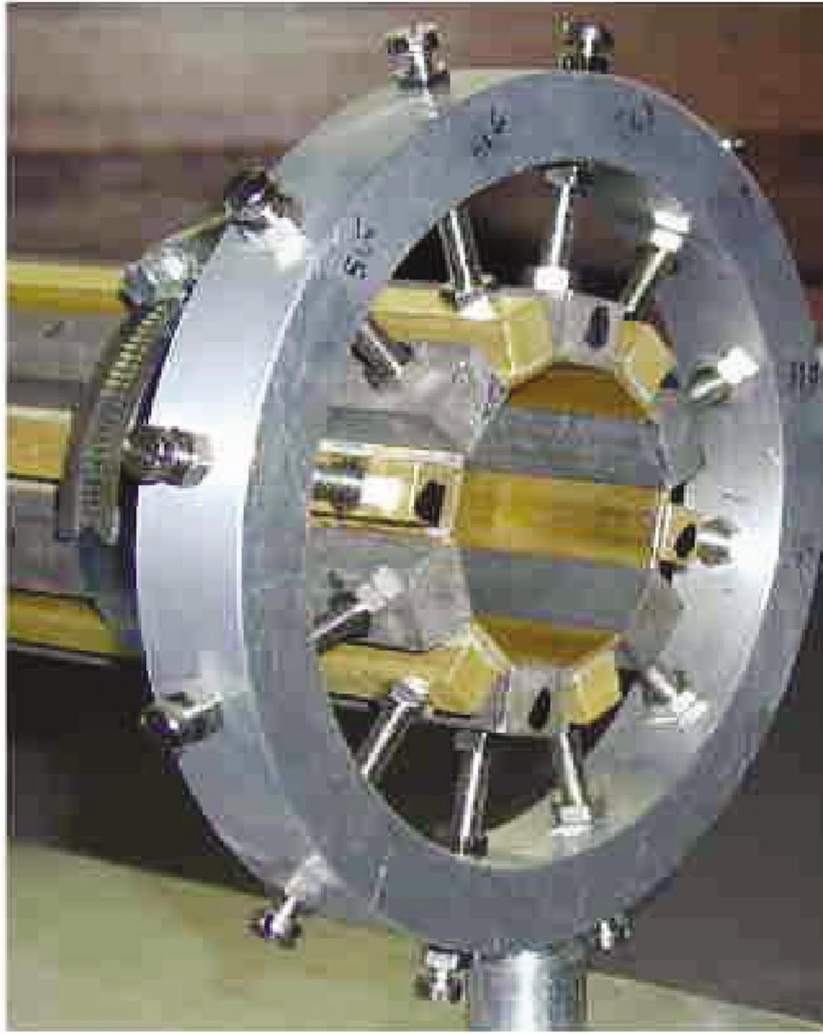


FIG. 8. (Color) Prototype used in the measurements.

bar (brass bar) with a steel bar will increase the losses in the resonator (since the current on the wall flows along a more resistive path) and a decrease of the resonance quality factor (Q factor) should be observed. The procedure used to measure the Q factor is described in Appendix C.

A number of measurements has been performed replacing brass bars with steel ones and eventually comparing the results from different configurations. In order to distinguish between different configurations we introduce a suffix indicating the number of steel bars mounted; for instance Q_N refers to the prototype when N steel bars and $(12 - N)$ brass bars are mounted (Q_0 refers to the situation with only brass bars). Typical measurements concern Q_0 , Q_1 , Q_2 , Q_3 . Since the steel bars are found to be remarkably different (geometrically and in their surface properties), they have been labeled (“bar 1,” “bar 2,” “bar 3”) and we refer to the Q factor measured with all brass except the steel “bar j ” ($j = 1, \dots, 3$) as Q_1^j . This sorting is necessary only for the steel bars while brass bars are treated as identical.

B. Measurement uncertainty

Each measured Q_i is the average of the Q factors obtained with different couplings. Following [16], the uncertainty u of a measurement result can be estimated with experimental standard deviation of the mean of repeated equivalent measurements (type A evaluation). Thus



FIG. 9. (Color) Q -factor measurements setup. The upper image shows the pipe connected to a network analyzer to measure (in transmission) the Q factor of the TEM resonator obtained inserting a silver-plated steel tube along the axis of the pipe (lower right photo). The bar is kept in the center by proper (white) Teflon supports which are perforated to perturb the field as little as possible. The left lower photo shows one of the two identical coupling electrodes (next to a matches box).

the measured value of Q_i is arithmetic mean \bar{Q}_i and its uncertainty

$$u(Q_i) = \sqrt{\frac{1}{M(M-1)} \sum_{j=1}^M (Q_{i,j} - \bar{Q}_i)^2}, \quad (46)$$

where $Q_{i,j}$ is one of the M realizations of the measurement of Q_i . Typical measured values for Q_0 , Q_1 , Q_2 , Q_3 are shown in Ref. [1]. For a given bar configuration, the uncertainty is within the 0.1% of the measured \bar{Q}_i value.

Measurements showed that such uncertainty is negligible with respect to the uncertainty due to mechanical tolerances or imperfections. To estimate it, a series of measurements were performed mounting and dismounting the setup but keeping electrically analogous configurations (e.g., mounting three steel bars in different azimuthal positions). The power loss should be identical and the different Q -factor values obtained are due only to mechanical tolerances in the bar profile. Measured data are reported in Ref. [1] and the resulting uncertainty is within the 2% of the measured \bar{Q}_i value. Anyway, this uncertainty value is well acceptable for the purpose of our measurements.

C. Measurement results

Denoting P_{inner} the power dissipated in the inner conductor, P^{brass} the power dissipated on a generic brass bar and P_j^{steel} the power dissipated on the steel bar j , one can see that $P_0 = P_{\text{inner}} + 12P^{\text{brass}}$ and

$$P_N = P_{\text{inner}} + (12 - N)P^{\text{brass}} + \sum_{j=1}^N P_j^{\text{steel}}, \quad (47)$$

where P_0 and P_N are the power loss when the pipe is made of all brass bars (0 steel bars) and when there are N steel bars, respectively. The difference $P_0 - P_N$ is independent from the power dissipated in the inner conductor, i.e.,

$$P_0 - P_N = \sum_{j=1}^N (P^{\text{brass}} - P_j^{\text{steel}}) = \sum_{j=1}^N (P_0 - P_1^j), \quad (48)$$

where P_j^{steel} is a fraction of the power loss on the steel bar j , while P_1^j is the power loss in all the cavity when there is one steel bar (namely the “bar j ”) and all the others are brass ones. Equation (48) is appealing because P_0, P_N, P_1^j can be measured easily. In fact the Q factor of a cavity is

$$Q = 2\pi f_0 \frac{W}{P},$$

where f_0 is the resonance frequency, P the power loss, and W the electromagnetic energy stored in the cavity. Assuming that f_0 and W remain “approximately” constant when changing 1 bar with another, then Eq. (48) becomes

$$\frac{Q_0 - Q_N}{Q_N} \approx \sum_{j=1}^N \frac{Q_0 - Q_1^j}{Q_1^j} \quad (49)$$

The resonance frequency remains more or less constant in any configuration as it can be verified during the measurements. The stored electromagnetic energy can also be considered constant (in a first approximation) provided that we refer to the energy stored inside the cavity, independently of the coupling circuit.

Therefore, to check the theoretical prediction of a constant magnetic field over the azimuth, we need to measure Q_0, Q_N , and Q_1^j and verify if the equality (49) is satisfied. Equation (49) is independent from the values of P_{inner} and even of the electrical properties of the single “bar j ” (provided that we measure Q_1^j and Q_N) [17]. The drawback is that we have to make at least four measurements (Q_0, Q_2, Q_1^1, Q_1^2) and then compare them. The result is prone to be affected by the mechanical tolerances which enters whenever we dismount a bar to substitute it with another one.

Each measured Q factor is affected by measurement artifacts, due mainly to mechanical tolerances, and its uncertainty has been estimated as discussed in Sec. V B. The effect of those uncertainties on the identity of Eq. (49) can be taken into account combining the uncertainties of each quantity involved, i.e., estimating the “combined uncertainty” u_c [16]. For convenience we label the left-hand side (lhs) and right-hand side (rhs) of Eq. (49) as f and g , respectively, and verifying Eq. (49) results in comparing \bar{f} and \bar{g} with the proper uncertainties $u_c(f)$ and $u_c(g)$, being

$$\bar{f} = \frac{\bar{Q}_0 - \bar{Q}_N}{\bar{Q}_N} \quad \text{with } u_c(f) = \frac{\bar{Q}_0}{\bar{Q}_N} \sqrt{\left[\frac{u(Q_0)}{\bar{Q}_0}\right]^2 + \left[\frac{u(Q_N)}{\bar{Q}_N}\right]^2}, \quad (50a)$$

$$\bar{g} = \sum_{j=1}^N \frac{\bar{Q}_0 - \bar{Q}_1^j}{\bar{Q}_1^j} \quad \text{with } u_c(g) = \sqrt{\left[\sum_{j=1}^N \frac{u(Q_0^j)}{\bar{Q}_1^j}\right]^2 + \sum_{j=1}^N \left(\frac{\bar{Q}_0}{\bar{Q}_1^j}\right)^2 \left[\frac{u(Q_1^j)}{\bar{Q}_1^j}\right]^2}, \quad (50b)$$

since Q_0, Q_N, Q_1^j ($j = 1, \dots, N$) are independent quantities.

Applying Eqs. (50) to the available measurements [1], the results are shown in Table I, where the bold values are the lhs and rhs of the identity (49) at the two measured resonance frequency and for the two bars configurations; the corresponding combined uncertainty u_c are also

TABLE I. Left-hand side term (f) and right-hand side term (g) of the identity (49) with their uncertainty.

		\bar{f}	$u_c(f)$	\bar{g}	$u_c(g)$
2 steel bars	288 MHz	0.704	0.018	0.687	0.031
	1.16 GHz	0.589	0.014	0.579	0.022
3 steel bars	288 MHz	1.037	0.016	1.041	0.034
	1.16 GHz	0.877	0.012	0.880	0.025

reported. In the four cases shown, the bold values in each line are very close; the difference between two corresponding values is always smaller than half of $\sqrt{u_c^2(f) + u_c^2(g)}$ which means that the two values can be considered identical within the measurement uncertainties and the identity (49) has been confirmed.

VI. HEATING POWER IN THE LHC BEAM SCREEN

The design of the copper-coated LHC beam screen is finished and its installation has already began. As stated before, the welding can be considered as a small strip of a bad conductor (approximately stainless steel), covering about 1/60th of the entire liner cross section.

Previous results have shown that, in a wide part of the LHC bunch frequency spectrum, the tangential magnetic field is constant along the boundary. Its value is close to the field of a charge in a perfectly conducting beam pipe, i.e., the first order term of a perturbative solution. This result is strictly valid provided that the skin depth is smaller than the screen thickness (which we have assumed infinite in our analysis).

Our theory deals with a cylindrical metallic beam pipe with a smoothly varying conductivity $\sigma(\phi)$ as in Eq. (17). The actual LHC beam screen has two main differences from our model. First of all the beam screen has a “steplike” change in the conductivity going from the copper one to the conductivity of the welding (which we can safely assume close to the stainless steel one). Moreover the cross section of the screen is not exactly circular but it is flattened at two opposite sides [1].

If the image currents are constant for a pipe with a smoothly varying conductivity, it is reasonable to assume it constant also in the LHC beam screen. The effect of the change in geometry (from the circular one to the real one) can then be estimated using the static field solution [18].

It has been shown in Ref. [1], that the heating power in the LHC flattened beam pipe can be computed by the heating power in a circular copper beam pipe (circumscribed to the real one) providing some geometrical correction factors. Those factors are ratios involving the radial electric field generated by a point charge in the two geometries (circular and flattened one) and they can be calculated solving (numerically) the Poisson equation in the actual flattened beam pipe.

The final results are shown in Ref. [1,2], assuming nominal LHC parameters. The small welding strip dissipates about 7% of the power dissipated in the copper-coated part at room temperature. At cryogenic temperatures, the effect is more pronounced (since the conductivity of the copper increases but the electric properties of the welding remain nearly unchanged) and the small strip dissipates about 34% of the power dissipated in the copper. Our analysis has confirmed previous estimates for heating power which were derived for a smaller beam screen radius but no welding strip [1].

This estimate is valid provided that the beam pipe wall thickness is greater than the skin depth at any relevant frequency. To account for finite wall thickness, i.e., field penetrating through the beam screen, one has to consider also the geometry outside the liner. A

possible approach to treat this problem could be a field matching analysis analogous to what has been done to estimate transverse beam coupling impedance for multilayered beam pipes [19].

VII. CONCLUSIONS

We have shown a general (semi)analytical approach to find the field generated by a charge traveling on axis in a metallic beam pipe whose admittance varies azimuthally with n sinusoidal oscillations.

Applying it to LHC beam screen case, we have shown that the magnetic field on the boundary is practically purely azimuthal ($H_\phi \gg H_z$) and it is constant over the azimuth down to very low frequency. Thus the same amount of current flows in the good conductor as in the bad one. Numerical simulations and bench measurements on a prototype confirm this prediction. Those results justified the use of first order perturbation theory: H_ϕ on the boundary can be assumed constant and equal to the charge field in free space. The fraction of power dissipated in the welding of the LHC beam screen can therefore be easily computed, both at room and at cryogenic temperature.

ACKNOWLEDGMENTS

The work reported in this paper has been done at CERN and it profited substantially of the help and the supervision of F. Ruggiero (CERN), of F. Caspers (CERN), and of Professor L. Palumbo (Università di Roma “La Sapienza”).

APPENDIX A: GREEN’S FUNCTION APPROACH IN KNOWN CASES

Before going through the detailed analysis of the effect of an azimuthal variation of the conductivity, we review a few well known cases in the framework of the formalism presented in Sec. II.

1. Charge in the free space

A charge Q traveling in the free space in the z -direction with a velocity βc is associated with a current density (in the frequency domain) of:

$$\mathbf{J}(r, \phi, z; \omega) = \hat{z} Q \frac{\delta(r)}{2\pi r} \exp\left(j \frac{k}{\beta} z\right). \quad (\text{A1})$$

The electric Hertzian potential does not depend on ϕ and it can be written as [1]

$$\Pi_{0z} = j \frac{Z_0 Q}{2\pi k} K_0\left(\frac{kr}{\beta\gamma}\right) \exp\left(j \frac{k}{\beta} z\right), \quad (\text{A2})$$

with γ being the relativistic factor. The fields are then easily obtained using Eqs. (2) with the only electric potential. In the ultrarelativistic regime, i.e., when the particle velocity approaches the speed of light ($\gamma \rightarrow \infty$), the only nonvanishing field components are the radial electric field and the azimuthal magnetic one:

$$E_r = j \frac{k}{\beta} \frac{\partial \Pi_{0z}}{\partial r} = Z_0 \frac{Q}{2\pi\beta} \frac{k}{\beta\gamma} K_1\left(\frac{kr}{\beta\gamma}\right) e^{jzk/\beta} \longrightarrow Z_0 \frac{Q}{2\pi r} e^{jzk/\beta}, \quad (\text{A3a})$$

$$E_z = -\frac{k^2}{\beta^2\gamma^2} \Pi_{0z} = -jZ_0 \frac{Q}{2\pi} \frac{k}{\beta^2\gamma^2} K_0\left(\frac{kr}{\beta\gamma}\right) e^{jzk/\beta} \longrightarrow 0, \quad (\text{A3b})$$

$$H_\phi = j \frac{k}{Z_0} \frac{\partial \Pi_{0z}}{\partial r} = \frac{Q}{2\pi} \frac{k}{\beta\gamma} K_1\left(\frac{kr}{\beta\gamma}\right) e^{jzk/\beta} \longrightarrow \frac{Q}{2\pi r} e^{jzk/\beta}. \quad (\text{A3c})$$

2. Charge in a perfectly conducting pipe

In a perfectly conducting pipe, the field will be the sum of the field of the charge in the free space (known) and a scattered field (unknown, for the moment), due to the presence of the perfectly conducting boundary; thus the total Hertzian potential will be as well the sum of the free space one (Π_{0z}) and of Π_{iz} which can be written as in Eq. (4a), namely

$$\Pi_{\text{TOT}z} = \Pi_{0z} + \frac{Z_0}{4\pi k} \int_{-\infty}^{\infty} F_0(\alpha) G_0(\alpha; r, b) e^{j\alpha z} d\alpha, \quad (\text{A4})$$

where only the monopole term $m = 0$ has been taken due to the symmetries (the charge is traveling along the z axis); $G_0(\alpha; r, b)$ is defined in Eq. (5). Applying the boundary condition, i.e., that the E_z is null at $r = b$, $F_0(\alpha)$ can be derived from a potential $\Pi_{\text{TOT}z}$ that is zero for $r \geq b$ and

$$\Pi_{\text{TOT}z} = j \frac{Z_0 Q}{2\pi k} \left[K_0(kr/\beta\gamma) - \frac{K_0(kb/\beta\gamma)}{I_0(kb/\beta\gamma)} I_0(kr/\beta\gamma) \right] \exp\left(j \frac{k}{\beta} z\right) \quad \text{for } r < b. \quad (\text{A5})$$

The well known properties of a charge traveling in a perfectly conducting pipe are easily found in Eq. (A5). First of all, there is no field inside the perfect conductor ($r > b$), since the Hertzian potential is zero; moreover $I_0(kr/\beta\gamma)$ tends to unity in the ultrarelativistic limit and thus the field generated by $\Pi_{\text{TOT}z}$ is identical to the one generated by Π_{0z} inside the pipe ($r < b$), since they differ only by a constant. Therefore inside a perfectly conducting pipe, the field of a relativistic charge is identical to the one in the free space, while it is zero for $r > b$: perfectly conducting walls “cut” the field lines. The surface current density, according to Eq. (7a), is [1]

$$J_{S_z} = -\frac{Q}{2\pi b} \frac{e^{jzk/\beta}}{I_0(kb/\beta\gamma)} \longrightarrow -\frac{Q}{2\pi b} e^{jzk} \quad \text{for } \beta \rightarrow 1. \quad (\text{A6})$$

The image current flowing in a perfect conductor (i.e., the integral of J_{S_z} along a generic circle of radius b) is equal in amplitude to the current of the charge, (that is the integral of J_z in Eq. (A1) over a generic surface normal to the propagation direction), but opposite in sign.

3. Charge in a uniformly conducting pipe

When the charge is moving in a pipe with finite, uniform conductivity σ , the Hertzian potential can still be written as in Eq. (A4), but with a different $F_0(\alpha)$ since the fields satisfy different boundary conditions (E_z is not anymore null on the boundary). Again, only the monopole term ($m = 0$) has an effect and this is related to the symmetry imposed by the uniform conductivity. To first order, the longitudinal electric field and the azimuthal magnetic one satisfy the SIBC discussed in Sec. II B, in particular, Eq. (8). Applying this condition, we find again an equation for $F_0(\alpha)$ which leads to the following expression for the total Hertzian potential:

$$\Pi_{\text{TOT}z} = j \frac{Z_0 Q}{2\pi k} \left[K_0(kr/\beta\gamma) - \frac{K_0(kb/\beta\gamma) - j \frac{\beta\gamma}{Z_0 Y} K_1(kb/\beta\gamma)}{I_0(kb/\beta\gamma) + j \frac{\beta\gamma}{Z_0 Y} I_1(kb/\beta\gamma)} I_0(kr/\beta\gamma) \right] e^{jzk/\beta}, \quad (\text{A7})$$

where $Y = 1/Z$ has been used. Such expression is meaningful only for $r < b$ since assuming

the SIBC, we implicitly assume a null field inside the conductor. In the limit of perfect conductor ($Y \rightarrow \infty$), Eq. (A7) becomes Eq. (A5), as it should be. All the fields can be, again, derived by the potential; in particular, the longitudinal electric field is nonvanishing and constant with r ; in fact for an ultrarelativistic charge Q

$$E_z = \frac{Q}{2\pi b} \frac{1/Y}{1 + jkb/(2Z_0 Y)} e^{jkz} \quad (\text{A8})$$

meaning that the traveling charge loses energy. Equation (A8) is a result well known in literature (see for example [13,20]).

APPENDIX B: VALIDITY OF THE TRUNCATED NUMERICAL SOLUTION

The values of the coefficients C_m, D_m, E_m, G_m in Eqs. (36) depend on the order L to which the system of Eqs. (29) is truncated. For instance, for a given tn , C_m is null if $L < tn$ (and the same holds for all the other coefficients); increasing L the coefficients approach their limit values with a velocity depending on the value of Y_n/Y_0 . An example is given in Fig. 10 for the coefficients E_m which have the slowest convergence; in the figure it is shown E_3 , which is zero for $L < 2$ and then increases up to its limit value faster for $Y_n/Y_0 = 0.76$ (black dots) and slower for $Y_n/Y_0 = 0.97$ (gray dots). The saturation value is reached for $L \approx tn + 15$ in the worst case: this is approximately true for every tn and can be used in the actual solution. Thus if the system of Eqs. (29) is truncated to a given order L only the coefficients up to $tn \approx L - 15$ (in the worst case) are accurate. Obviously also the quantities directly involved in the field expressions of Eqs. (21) have the same saturating behavior with L as shown in the right plot of Fig. 10 for H_ϕ^0 ; the convergence is somehow faster because also the coefficients other than E_n are involved [Eq. (42)]. Both E_3 and H_ϕ^0 are plotted normalized to their limit value.

For a given value of Y_n/Y_0 , the accuracy of the solution of the system depends on the number of terms included (which we will call L from now on) and the order up to which the coefficients are calculated L' (and L' should be at least $\approx L + 15$ in the worst case). To assess the reliability of the truncation order L , we have introduced the quantities \mathcal{E}_ϕ and \mathcal{E}_z in Eqs. (43) and (44). The solution may be considered reliable for a given order L , if $\mathcal{E}_\phi, \mathcal{E}_z \ll 1$. Increasing L , that is including more terms in the solution, \mathcal{E}_ϕ and \mathcal{E}_z can be made as small as desired. An example is shown in Fig. 11 for $Y_n/Y_0 = 0.76$ at the frequency of 1 GHz and for $n = 1$; terms up to order $L = 10$ are included, resulting in $\mathcal{E}_\phi < 10^{-3}$ and $\mathcal{E}_z < 10^{-2}$. It is worth mentioning that \mathcal{E}_ϕ and \mathcal{E}_z are sinusoidal functions of $L\phi$, as expected. For different frequencies, the maximum value of the errors is roughly of the same order (improving a little bit going to very small frequencies).

To get the same order of magnitude of \mathcal{E}_ϕ and \mathcal{E}_z with a higher conductivity jump, one should increase L . Figure 12 shows the situation for $Y_n/Y_0 = 0.97$ where a much higher number of

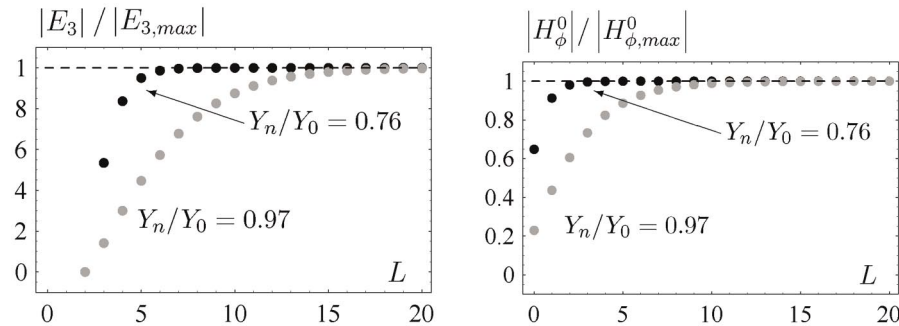


FIG. 10. Convergence of the coefficients (normalized to their limit value) of the final solution as a function of the truncation order L at 1 GHz and for two different conductivity jumps. ($b = 2$ cm, $n = 1$)

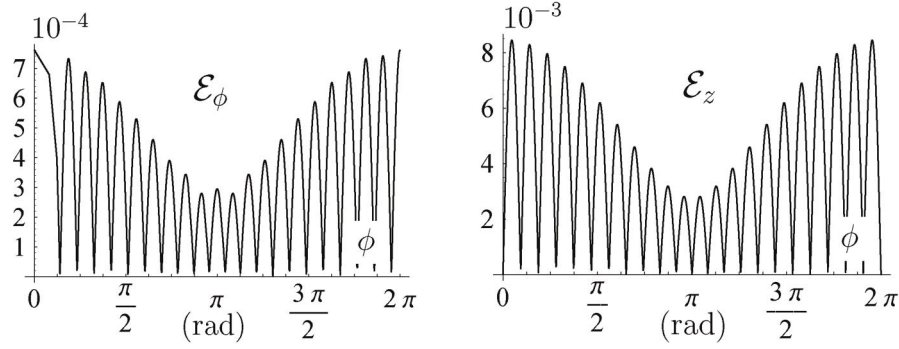


FIG. 11. \mathcal{E}_ϕ and \mathcal{E}_z for $Y_n/Y_0 = 0.76$ at 1 GHz; $L = 10$ but the coefficients are calculated at the order $L' = 16$. ($b = 2$ cm, $n = 1$)

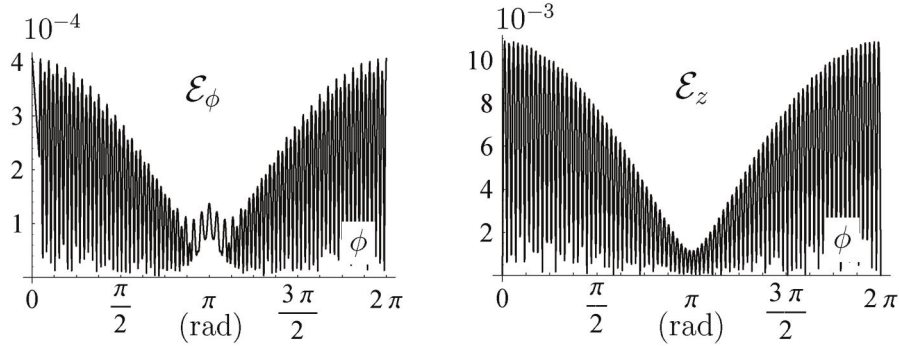


FIG. 12. \mathcal{E}_ϕ and \mathcal{E}_z for $Y_n/Y_0 = 0.97$ at 1 GHz; $L = 42$ but the coefficients are calculated at the order $L' = 60$. ($b = 2$ cm, $n = 1$)

terms ($L = 42$) is needed to keep $\mathcal{E}_\phi < 10^{-3}$ and $\mathcal{E}_z \lesssim 10^{-2}$. Again, changing frequency, more or less the same number of coefficients is needed to keep \mathcal{E}_ϕ and \mathcal{E}_z constant.

APPENDIX C: Q -FACTOR MEASUREMENT TECHNIQUE

To rf power dissipation are inversely proportional to the Q -factor of the TEM resonator. In our setup, the Q factor is measured in transmission with a network analyzer (HP8753D); the value from the instrument depends on the coupling network and on the real Q factor of the TEM resonator, which eventually we want to measure (Q_{unload}). The theoretical expectations for the Q -factor concern, obviously, only Q_{unload} values.

In transmission type measurements, for symmetrical coupling [1]

$$Q_{\text{unload}} = \frac{Q_{\text{load}}}{1 - S_{12}(f_0)}, \quad (\text{C1})$$

where Q_{load} is the Q factor read directly from the network analyzer display (when set in “automatic Q measure” configuration). The $S_{12}(f_0)$ is the transmission coefficient S_{12} at the resonance frequency f_0 ; usually the magnitude of $S_{12}(f_0)$ is expressed in decibels and called “insertion loss” α_L (that is the “Loss” reading of the network analyzer display). Because $S_{12}(f_0)$ is always smaller than unity, α_L is a negative number. The accuracy of Eq. (C1) is seriously reduced when the coupling is strong (i.e., little power is dissipated in the coupling circuit) since $S_{12}(f_0)$ approaches to unity, but it was not the case in our measurements.

The validity of Eq. (C1) requires the couplings at the two ports being symmetrical. This can be “electrically” checked by measuring the reflection parameters S_{11} and S_{22} . The distance

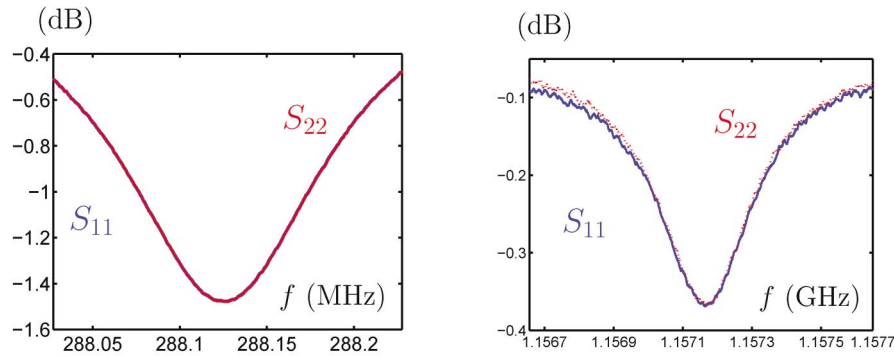


FIG. 13. (Color) S_{11} (blue solid line) and S_{22} (red dashed line) for a typical Q -factor measurement at the two resonant frequencies.

between the disk and the brass cylindrical plugs is fixed and equal for the two couplers. Moving back (forward) the couplers, the corresponding reflection S -parameter will decrease (increase). The symmetrical coupling is ensured when, in a given frequency span around the resonance frequency, the S_{11} and S_{22} curves are identical, as shown in Fig. 13 for the two frequencies at which we performed the measurements. The left plot refers to the resonance at 288 MHz and the frequency span in which we seek the identity of S_{11} and S_{22} is 200 kHz; the right plot refers to the resonance at 1.16 GHz and the frequency span is of 1 MHz.

Therefore, a typical Q -factor measurement for a given configuration of the bars at a resonant frequency f_0 consists of the following steps:

- (i) adjust the distance between the couplers and the inner conductor to get symmetric coupling which is met when $S_{11} = S_{22}$ on the predefined frequency range;
- (ii) record the Q -factor value (that is Q_{load}), the loss value α_L to get $S_{12}(f_0)$ and then compute Q_{unload} with Eq. (C1);
- (iii) repeat this procedure for several values of maximum variations of the reflection parameters (for instance 0.1, 0.3, 0.5, 0.7, 0.9 and 1.1 db), that is for different (but always symmetric) couplings. The resulting Q_{unload} should be constant.

-
- [1] A. Mostacci, Ph.D. thesis, Università di Roma “La Sapienza,” 2001; Report No. CERN-THESIS-2001-014, 2001 (unpublished).
 - [2] F. Caspers, A. Mostacci, L. Palumbo, and F. Ruggiero, in *Proceedings of the Particle Accelerator Conference, Chicago, IL, 2001* (IEEE, Piscataway, NJ, 2001); CERN LHC Project Report No. 493, 2001 (unpublished).
 - [3] L. Palumbo, *Part. Accel.* **25**, 201 (1990).
 - [4] E. Gianfelice and L. Palumbo, *IEEE Trans. Nucl. Sci.* **37**, 1084 (1990).
 - [5] L. Palumbo and V.G. Vaccaro, in *Proceedings of the CERN Accelerator School: Advanced Accelerator Physics Course, Oxford, 1985*, edited by S. Turner (CERN Yellow Report No. 87-03, 1987).
 - [6] L. A. Weinstein, *The Theory of Diffraction and the Factorization Method* (Golem Press, Boulder, 1969).
 - [7] R. E. Collin, *Field Theory of Guided Waves* (IEEE, New York, 1991), 2nd ed.
 - [8] T. B. A. Senior and J. L. Volakis, *Approximate Boundary Conditions in Electromagnetics* (The Institute of Electrical Engineers, London, 1995).
 - [9] D.-S. Wang, *IEEE Trans. Antennas Propag.* **35**, 453 (1987).
 - [10] Sharp variation of the conductivity (e.g., very thin welding in the LHC beam pipe) may result in a surface impedance not satisfying Eq. (11) and second (or higher) order boundary conditions must be used [8]. We will not deal with this case, but the method proposed here can be extended at the price of an increase of the complication of the analytical or numerical solution.
 - [11] In the following, the “Einstein” summation rule over repeated indexes is assumed.

- [12] A. W. Chao, *Physics of Collective Beam Instabilities in High Energy Accelerators* (Wiley-Interscience, New York, 1993).
- [13] B. W. Zotter and S. A. Kheifets, *Impedances and Wakes in High-Energy Particle Accelerators* (World Scientific, Singapore, 1998).
- [14] A. B. Pippard, Proc. R. Soc. A **191**, 385 (1947).
- [15] See World Wide Web address, www.ansoft.com
- [16] International Organization for Standardization *et al.*, *Guide to Expression of Uncertainty in Measurement* (ISO, Geneva, 1995), p. 101.
- [17] This is very relevant for the steel bars because the steel has also magnetic properties ($\mu_r \neq 0$) which cannot be easily estimated at the measurement frequency. In fact in our setup, we used (for convenience) the kind of steel used in civil construction and its magnetic properties are not reported in the data sheets.
- [18] F. Ruggiero, CERN SL/95-09 (AP), LHC note 313, 1995; in *Proceedings of the Workshop on Collective Effects in Large Hadron Colliders, Montreux, 1994*, edited by E. Keil and F. Ruggiero [Particle Accelerators 50, 83 (1995)].
- [19] E. Keil and B. W. Zotter, Report No. CERN-SL-98-019-AP, 1998 (unpublished).
- [20] G. Stupakov, Report No. SLAC-PUB-8208, 1999 (unpublished).